Fluid Dynamics &
Materials Processing

Tech Science Press

http://doi.org/10.32604/fdmp.2026.073927

ARTICLE

Base Flow Control through Bullet-Shaped Ribs at Mach 1.6

Uzma Anis Takkalki[1], Sayed Ahmed Imran Bellary[2], Sher Afghan Khan[3], Abdul Aabid[4,*] and Muneer Baig[4]

[1]Department of Space, School of Engineering, Ajeenkya DY Patil University, Pune, Maharashtra, India
[2]Department of Robotics and Automation Engineering, Zeal College of Engineering and Research, Narhe, Pune University, Pune, Maharashtra, India
[3]Department of Mechanical & Aerospace Engineering, Faculty of Engineering, IIUM, Kuala Lumpur, Malaysia
[4]Department of Engineering Management, College of Engineering, Prince Sultan University, Riyadh, Saudi Arabia
*Corresponding Author: Abdul Aabid. Email: aaabid@psu.edu.sa

Received: 28 September 2025; Accepted: 03 April 2026; Published: 07 May 2026

ABSTRACT: The rapid development of space transportation systems and high-speed military aircrafts have intensified interest in turbulent separated flows, particularly under transonic and supersonic conditions. Such flows commonly arise downstream of sudden expansions, where separation and subsequent reattachment generate strong shear layers, increased drag, and a low-pressure recirculation region at the base. In this study, the control of base pressure downstream of a sudden expansion is investigated numerically using a passive bullet-shaped rib. A jet issuing from a nozzle is discharged abruptly into a duct of 25 mm diameter, producing a separated flow with pronounced recirculation. Bullet-shaped ribs with length-to-diameter ratios ranging from 0.5 to 3 are placed at different axial locations, and three rib geometries are examined. The results indicate that ribs with L/D = 0.5 are largely ineffective for two of the geometries, whereas the third geometry produces a substantial increase in base pressure. For rib placements at L/D ratios of 1, 1.5, and 2, geometries corresponding to cases 1 and 2 do not significantly alter the flow, as reattachment occurs farther downstream. In contrast, the rib geometry of case 3 consistently enhances base pressure across all tested locations, with the most pronounced improvements observed when the rib is positioned at L/D = 2 and 3.

KEYWORDS: Bullet-shaped rib; L/D ratio; MPR; Mach (M); sudden expansion; base drag

1 Introduction

The turbulence has persisted as an unresolved enigma. It occurs in both natural and engineered flows around us, making it vital to understand. Managing turbulence-induced drag requires knowing its basics. In some cases, turbulence can be beneficial, like in fluid mixing. However, in engineering, turbulence is usually unwanted and should be minimized to save energy. Turbulent drag has significant effects on ecosystems and economic costs. Various methods are employed to enhance the efficiency of fossil fuels.

Expanded flow fields are used across practical and engineering contexts, including parallel diffusers, propulsion systems, and combustion chambers. These flows are studied primarily because of the need for control. Since they achieve desired outcomes without relying on additional mechanisms, such as active control, passive control methods have been favored by scientists for their simplicity and ease of implementation. Passive control has limitations, especially compared with launch vehicles, which are discarded once their propellant is fully consumed. A key advantage of dynamic control is its flexibility, which allows it to be used as an essential tool.

Many applications, such as military aircraft, jet engines, rockets, gas pipelines, and abrasive milling, rely on the principles of compressible flow. Therefore, current literature provides extensive information on sudden expansion issues, focusing mainly on specific scenarios involving flow and geometric parameters for such application. Reducing turbulent drag can help mitigate global warming by lowering CO_2 emissions from fossil fuel combustion. Therefore, efforts should aim to eliminate near-wall organized structures that significantly increase drag. Passive techniques such as splitter plates, riblets, Gurney flaps, bleed, and superhydrophobic surfaces are relatively easy to implement but offer limited drag reduction. In contrast, active control methods can achieve substantial reductions in skin friction drag. Although active control strategies are complex and require feedback systems, exploring innovative options in this area remains promising.

2 Literature Review

At Mach numbers greater than unity, the flow field shows complex contours, including flow partition, recirculation regions, and base pressure shortfalls, all of which substantially increase aerodynamic drag. Many researchers have studied passive control techniques, such as ribs, cavities, and other shapes, to address these concerns and improve base pressure. Khan et al. [1] investigated how ribs act as passive control methods that affect base pressure for Mach M = 1. They found that flow regulation significantly increased base pressure by disrupting the recirculation sector and encouraging early flow reattachment. Exploring different rib shapes, Khan et al. [2] conducted simulations of flows at Mach 1, providing insights into velocity profiles and changes in base pressure. The research underscored the critical roles of nozzle geometry and expansion ratios in determining flow behavior.

Advances in computational fluid dynamics (CFD) have enabled more detailed analyses. Khan et al. [3] conducted a CFD study on base pressure control using quarter ribs in sudden expansion ducts at critical Mach numbers. Their findings showed that quarter ribs efficiently control the flow, increasing base pressure and reducing drag. Li et al. [4] highlighted the processes involved in managing base flows. Passive controls typically employ geometric modifications to the enlarged duct, such as cavities and ribs, that alter jet control to influence shear-layer stability and serve as flow-control measures. These passive methods generally entail minimal cost and are easier to implement. Cavities, including base and ventilated types, are among the most common flow-control technologies for managing flow in suddenly expanded systems and can reduce the base pressure required by organizational specifications. Rathakrishnan et al. [5] studied flow through a circular duct with regularly spaced cavities, finding that cavity circulation reduces flow oscillations in the duct, allowing smoother pressure growth from low to ambient at the exit. Pandey and Rathakrishnan [6] extended this assessment to multiple-aspect-ratio cavities, noting that cavity effects are significant, especially in longer ducts compared to shorter ones.

Vikramaditya et al. [7] conducted an experimental analysis to examine how the base cavity responds to pressure variations in the base segment of a traditional missile traveling at Mach M = 0.7. The foremost goal was to identify pressure changes and their key drivers. Due to the highly non-uniform flow, they observed that the pressure variation features at the base differed significantly across azimuthal directions because of the model's asymmetry. They also noted that adding a base cavity promotes a sustained rise in base pressure. Additionally, the cavity's geometric dimensions play a crucial part in determining base pressure. Baig et al. [8] explored the use of base flows via microjets, demonstrating that active control methods can effectively manage base pressure and decrease drag. Rehman and Khan [9] devoted considerable attention to the use of micro-jets to control base pressure, offering valuable insights into the design and application of dynamic flow control methods. Using computational fluid dynamics, Rao et al. [10] investigated the flow characteristics within CD nozzles.

Their findings highlighted the critical importance of accurate boundary conditions for obtaining reliable flow predictions. Najar et al. [11] compared the functioning of the k-ε and Spalart–Allmaras turbulence models in compressible flows through convergent-divergent nozzles, where significant density variations occur. Their results showed that the k-ε model provided superior estimates of flow behavior and reattachment location. Using a homogeneous equilibrium model, Salvador et al. [12] examined cavitation phenomena in convergent-divergent diesel injector nozzles. The study highlighted the critical role of accurate cavitation modelling in understanding and optimizing injector performance and design. Pushpa et al. [13] examined heat transfer and buoyancy-driven convection in copper-water nanofluids within an annular cavity fitted with a thin baffle. Their findings demonstrated that incorporating nanofluids significantly enhanced heat transfer performance. Koomullil et al. [14] proposed a robust, generalized mesh generation framework for CFD applications. The approach enabled accurate simulation of complex flow phenomena across a wide range of intricate geometries.

Rathakrishnan [15] conducted experiments using a converging nozzle followed by a sudden expansion at different primary pressure ratios, with three quadrilateral control mechanisms having w:h ratios of 3:1 to 3:3. He positioned five rectangular ribs inside a 12.5 mm-radius duct at 1D each. Outcomes indicated that for an aspect ratio (3:1), the base pressure decreases, whereas a taller height of 3 mm tends to increase it. These findings primarily functioned as yardsticks, and CFD simulations were used to reproduce them. After confirming the CFD results, the author concluded that five ribs are redundant; one rib could generate analogous results without affecting pressure in the base area. The study later employed a bullet-shaped rib to control the base pressure. This research demonstrates passive management of base pressure in a 25 mm diameter pipe at M = 1.6 using bullet-shaped ribs.

3 Finite Volume Method

In this work, the finite volume method is used to simulate the model and analyze the results. This section explains the detailed design from geometry to a complete mesh model with appropriate boundary conditions. Additionally, the current work includes the mesh-independence test and validated it against existing experimental data.

3.1 Geometry and Modelling of CD Nozzles

The finite-volume technique was utilized to investigate this topic. CFD was performed using ANSYS FLUENT 2024/R2 to assess the flow through the nozzle [14,15]. The study used the Reynolds-averaged Navier–Stokes (RANS) equations with the k-ε turbulence model. We have examined the impact of the bullet's shape on the rib using a passive method. The different orientations of the bullet-shaped rib are shown in Fig. 1.

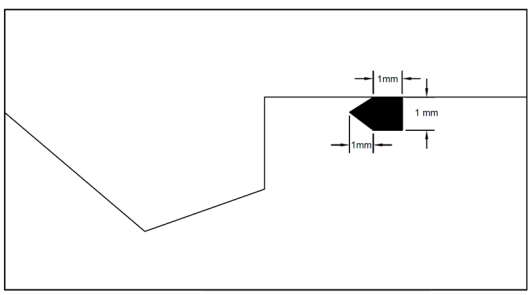

(**a**) Case 1

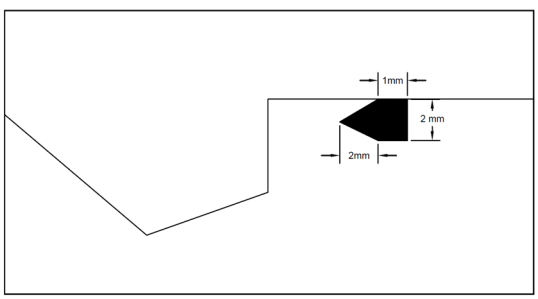

(**b**) Case 2

Figure 1: *Cont.*

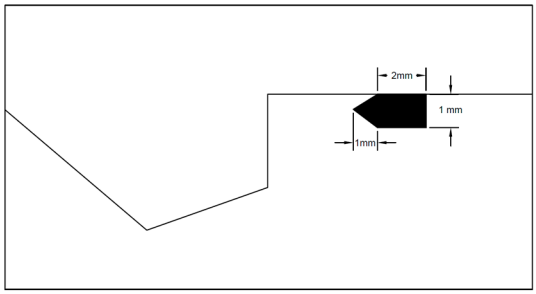

(**c**) Case 3

Figure 1: Nozzle and duct assembly with different parameters of the control geometry.

3.2 Meshing and Boundary Conditions

A significant step in CFD is meshing. Using the free-face mesh type, the 2-D model employs a structured mesh. Element sizes were assigned based on the lengths of each line (edge), which guided the mesh creation. These lines determined the element sizes, and elements with similar shapes were generated via face-meshing. A mesh independence test was performed. Fig. 2 illustrates the element types and sizes used during this check. The mesh independence test for the 25 mm duct without a rib (L/D = 6) involved various element sizes, all based on the same geometry. Ten thousand iterations were performed for convergence, with a residual threshold of 1×10^{-6} for continuity, momentum, and turbulence equations.

A steady-state density-based solver was employed for the 2D model. The density-based implicit formulation was applied to simulate turbulent flow regimes where low-speed flow effects were not dominant. Because the governing equations are nonlinear and strongly coupled, multiple iterations are required to achieve convergence. These equations are linearized in terms of the dependent variables, and the unknown quantities are computed for each computational cell [16].

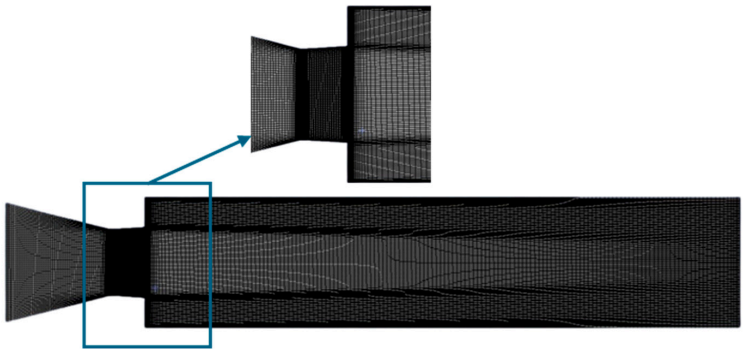

(**a**) No Control

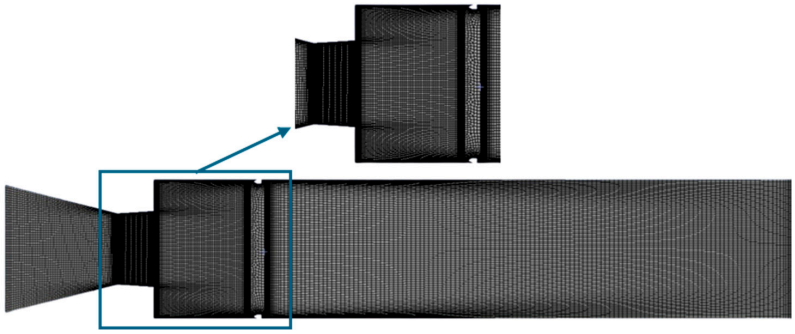

(**b**) Case 1

Figure 2: *Cont.*

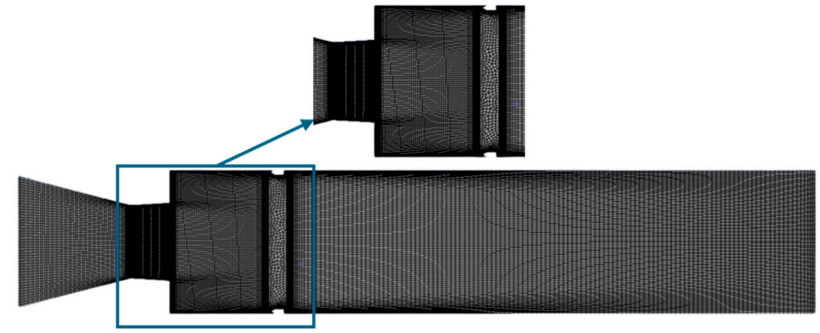

(**c**) Case 2

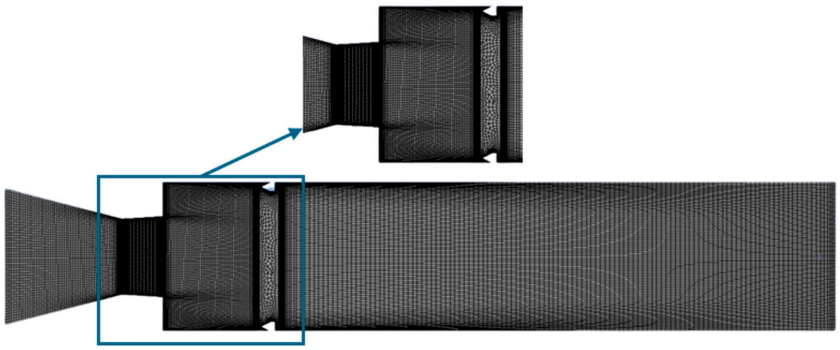

(**d**) Case 3

Figure 2: ANSYS simulation model.

3.3 Assumptions and Fluid Properties

Conventions are used to accurately represent flow behavior in natural situations, with suitable scientific and arithmetical models chosen to simplify the most fundamental expressions.

To resolve the governing equations concurrently, numerical modelling involves selecting appropriate mathematical models, specifying boundary conditions, ensuring mesh quality, and selecting a simulation methodology. Although it cannot precisely capture physical events, this computational technique has been relied upon for years and provides valuable insights into stream patterns. Therefore, it's essential to select elements that carefully mimic the actual flow. This research identifies assumptions that may compromise the accurate representation of the physical condition. The next section outlines the assumptions and features discussed in this study.

i. The stream is well-designed to be a stable 2D flow owing to the geometry's symmetry. Therefore, the hypothesis that the stream is two-dimensional is correct.
ii. The flow is compressible, so the density will change with the inertia parameters. The inlet pressure is a gauge pressure that corresponds to the Mach number and NPR, while the exit pressure is zero.
iii. The turbulent stream plays a significant role in turbulent viscous degeneracy at a specific flow speed, so it is considered.
iv. The viscosity of the air depends on temperature.
v. At the usual ambient pressure, it is assumed to be at the tube exit.

As the flow is turbulent, a variable-density flow field is modelled using the standard k-ε model. The following expressions are most appropriate for describing the flow.

The continuity equation for compressible flow is as follows:

The steady continuity equation is as follows:

$$\underline{\nabla} \cdot (\rho \underline{V}) = 0 \tag{1}$$

The flow velocity is represented by V.

The expression for momentum conservation is:

$$\underline{\nabla} \cdot (\rho \underline{V V}) + \underline{\nabla} p = \underline{\nabla} \cdot \left[2\mu (\underline{\nabla V})_o^s\right] + \underline{\nabla} \cdot (\tau_{=Re}) \tag{2}$$

where $(\underline{\nabla V})_o^s = (\underline{\nabla V})^s - \frac{1}{3}(\underline{\nabla} \cdot \underline{V})\underline{I}$, $(\underline{\nabla V})^s = \frac{\underline{\nabla V} + \underline{\nabla V}^T}{2}$, and $\tau_{=Re}$ is the turbulent stress tensor.

The general expression for overall energy is as follows:

$$\frac{\partial}{\partial t}\left[\rho\left(\frac{1}{2}V^2 + u_{int}\right)\right] + \underline{\nabla}\left[\rho\left(\frac{1}{2}V^2 + u_{int}\right)\underline{V}\right] = \underline{\nabla}\left(\lambda \underline{\nabla} T - p\underline{V} + 2\mu \underline{V} \cdot (\underline{\nabla V})_o^s + \underline{V} \cdot \tau_{=Re}\right) \tag{3}$$

where u_{int} is the internal energy, and λ is the thermal conductivity.

The k-epsilon turbulence model is appropriate for internal flows, is robust, and provides adequate precision. The Ansys Fluent module within the Ansys Workbench 2024/R2 software suite incorporates the k-epsilon (ε) turbulence model used in the present study. The k-equation permits us to compute the turbulent kinetic energy.

$$\frac{\partial}{\partial t}(\rho k) + \underline{\nabla} \cdot (\rho \underline{V} k) = \underline{\nabla} \cdot \left[\left(\mu + \frac{\mu_t}{\sigma_k}\right)(\underline{\nabla} k)\right] - \rho\varepsilon + \mathrm{M_x} \tag{4}$$

The turbulent KE degeneracy rate is designated by ε, the turbulent Prandtl number is σ-k, and $\mathrm{M_x}$ is the turbulence creation.

$$\frac{\partial(\rho\varepsilon)}{\partial t} = -\underline{\nabla} \cdot \left(\rho\varepsilon \vec{V}\right) + \underline{\nabla} \cdot \left[\left(\mu + \frac{\mu_T}{\sigma_\varepsilon}\right)\nabla\varepsilon\right] - C_1 f_1 \left(\frac{\varepsilon}{k}\right) M - C_2 f_2 \frac{\varepsilon^2}{k} \tag{5}$$

where $\mu_t = \rho f_\mu C_\mu k^2/\varepsilon$ denotes turbulent viscosity, and the random constants are denoted as $\overline{C_\mu} = 0.09$, $\overline{C_1} = 1.44$, $\overline{C_2} = 1.92$, $\overline{f_\mu} = 1$, $\sigma_k = 1.0$, and $\sigma_\varepsilon = 1.3$.

3.4 Authentication of Investigational Model

The ANSYS Workbench employed fluid-flow analysis techniques (Fluent). It was built using the Design Modeler. Rathakrishnan [15] used an experimental setup consisting of a convergent nozzle connected to an enlarged duct. The flow accelerates through the nozzle and then suddenly expands into the duct fitted with five ribs. The details of this model are presented in Table 1.

Table 1: Details of the validation model.

Variables	Magnitudes
Inlet Nozzle radius	15 mm
Exit Nozzle radius	5 mm
Duct radius	12.5 mm
Duct Span	Differs from 1D to 6D
Converging span	20 mm
Rib breadth	3 mm
Rib height	Differs from 1 mm to 3 mm

Fig. 3 presents the base pressure data from both existing and prior studies [15]. Dotted lines represent experimental values, while solid lines show simulation results obtained with ANSYS Fluent. The numerical analysis in this work differed by less than 10% from the earlier experimental test, indicating that it met the acceptance criteria. The curves demonstrated a steady pattern, with individual points closely following one another. As shown in the table and graph discussed earlier, the validation of this effort was effective. As per the study by Rathakrishnan [15], prior research examined w/h ratios ranging from 3:1 to 3:3; a duct diameter of 25 mm; L/D ratios from 1 to 6; and NPRs of 1.141 and 2.458. In an earlier periodical by Rathakrishnan [15], results from Fig. 3 containing an NPR of 2.458 and models with rib control for w:h ratios of 3:2 and 3:3 that were selected for assessment with this study. The simulations are supported by Rathakrishnan's [15] test data, which included five equally spaced ribs inside the tube, as depicted in Fig. 3. These outcomes include fluctuations in base pressure at NPR 2.458 and L/D ratios from 1 to 6. The study was repeatable, verifying the numerical results for models with rib control at numerous aspect ratios [15].

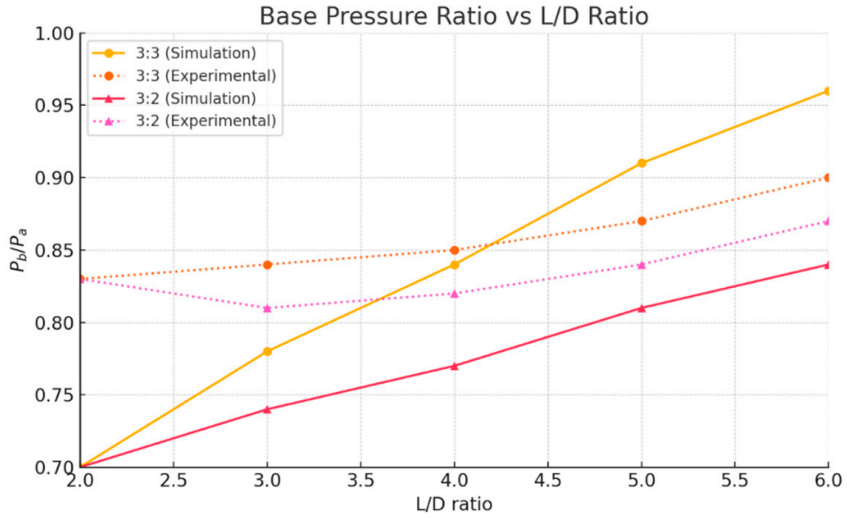

Figure 3: Authentication of earlier work.

3.5 Mesh Convergence Test

In supersonic nozzle flows at moderate Mach numbers 1.6 to 1.68 for the mesh convergence test, the flow is generally shock-free in the divergent section if well-resolved and properly expanded, and the exit Mach number, centerline exit velocity, and exit static pressure are highly sensitive to mesh resolution in the divergent region due to accurate capture of expansion waves and boundary layers. Global quantities like mass flow rate or thrust coefficient converge faster. Based on Table 2, the percentage variations are computed relative to the finest mesh (reference = 0%). A typical convergence criterion is <1% change between fine and finest meshes. Table 2 presents a mesh-independence analysis, which is essential for confirming that the simulation outcomes are not affected by grid refinement. The meshes vary from coarse to fine, with each configuration listing the number of nodes and elements. As the mesh becomes finer, the number of nodes and elements increases significantly from 3235 in the coarsest mesh to 1,472,691 nodes and 1,469,434 elements in the finest mesh. The objective is to choose a mesh that provides sufficient accuracy while avoiding excessive computational load. Typically, finer meshes enhance detail but are computationally expensive, whereas coarse meshes are less precise but cheaper. Medium or fine meshes strike a practical balance between accuracy and efficiency.

Table 2: Mesh independence examination.

Mesh Level	Coarsest	Medium	Fine	Finest
Number of Cells/Elements (2D Axisymmetric)	3235	18,104	102,928	1,469,434
Exit Mach Number	1.68	1.62	1.6	1.6
% Variation in Exit Mach	5.00%	1.30%	0.00%	0.00%
Exit Velocity (m/s)	545	528	525	523
% Variation in Exit Velocity	4.20%	0.90%	0.00%	0.00%
Exit Static Pressure (Pa)	8689	8710	8720	8727
% Variation in Exit Pressure	−0.43%	−0.19%	0.00%	0.00%

4 Results and Discussion

The base pressure, calculated numerically, is converted to absolute pressure by adding backpressure, and the resulting pressure is normalized by dividing it by the backpressure. The inertia parameter in this study is M = 1.6, and the design NPR is 4.25, indicating that the nozzle is perfectly expanded at that NPR. Values below 4.25 indicate over-expansion, while values above 4.25 indicate under-expansion. As NPR increases, the under-expansion level rises as well. Simulations cover NPR values from 3 to 11, increasing in steps of 2, with expansion levels of Pe/Pa 0.71, 1.18, 1.65, 2.12, and 2.59. To regulate flow within the duct, a bullet-shaped rib was used in three cases. In case 1, all dimensions of the triangular and rectangular parts, as well as the width, are 1 mm. In case 2, the conical length and width are 2 mm, while the rectangular length remains 1 mm. In case 3, the conical length and width are both 1 mm, and the rectangular length is 2 mm.

4.1 Base Pressure Outcomes for Rib Positioned at L/D = 0.5

Results for three different rib geometries, discussed earlier, were obtained at L/D = 0.5 for NPRs from 3 to 11 and for duct dimensions from L/D = 1 to 6, as shown in Fig. 4a. In the no-control scenario with L/D = 1, the base pressure is approximately 0.62 at NPR = 3. The pressure magnitude declines continuously, stabilizing at NPR = 5, which exceeds the required NPR for proper expansion. As NPR increases beyond 5, the base pressure ratios rise again for values of 6 or higher. The inertia level, flow relief, and rib placement influence this behavior. For larger duct diameters, this method makes the NPR effect on base pressure less relevant. Nevertheless, for NPR values of 6 or higher, the expansion level continues to affect the base pressure, and flow control remains highly effective.

When the control is employed, the diminishing tendency in the base pressure ratio persists until NPR equals 5. For NPRs greater than 5, a significant growth in the base pressure ratio is observed for rib geometries in cases 1 and 2, with a maximum value of 0.7. However, for the case 3 rib, the decreasing trend disappears, and from NPR = 3 onward, the base pressure increases. Nevertheless, as long as the nozzles are over-expanded, the control reduces the base pressure. Nonetheless, from NPR 4.25 onwards, the design NPR, the flow regulation results in a rise in the base pressure ratio, reaching a maximum of 0.9. Still, these control mechanisms cannot raise the base pressure. These results reiterate that, whether dynamic or inactive, the control is beneficial when the nozzles are exposed to a favorable pressure gradient.

For the pipe span L/D = 2, the outcomes of the present investigations are nearly the same, except at NPR = 11, where the ribs for cases 1 and 2 differ, despite their effectiveness being the same, as seen in Fig. 4b. These variations may be due to ambient pressure effects on the duct size at an L/D ratio of 2. Analogous outcomes are observed in Fig. 4c–f, with marginal variations at smaller tube sizes (L/D = 1 to 4 and beyond). Even the earlier marginal variations have disappeared, as the reattachment appears to occur at L/D = 3 for this enlarged duct diameter. It is well known that when the flow is connected to the duct, any subsequent increase in the duct length does not affect the flow field.

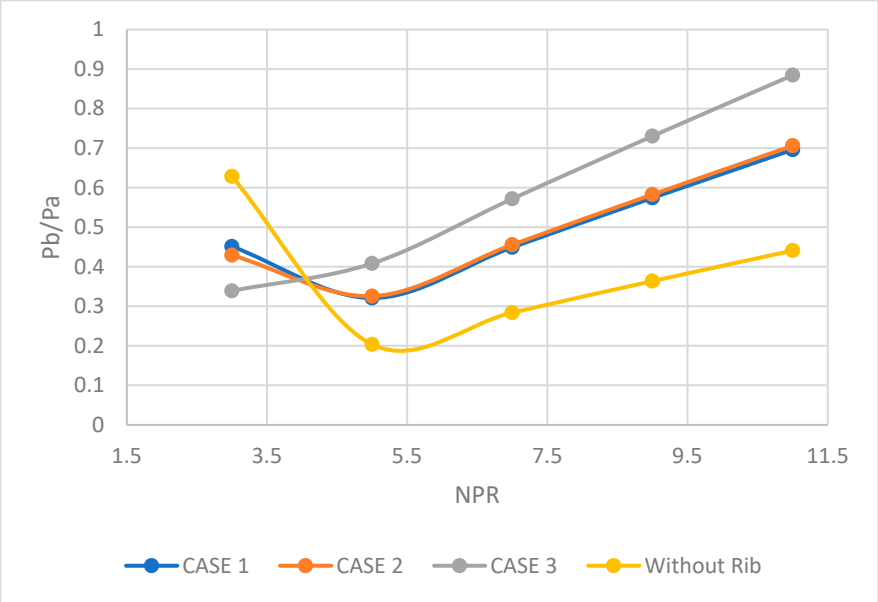

(**a**) L/D = 1

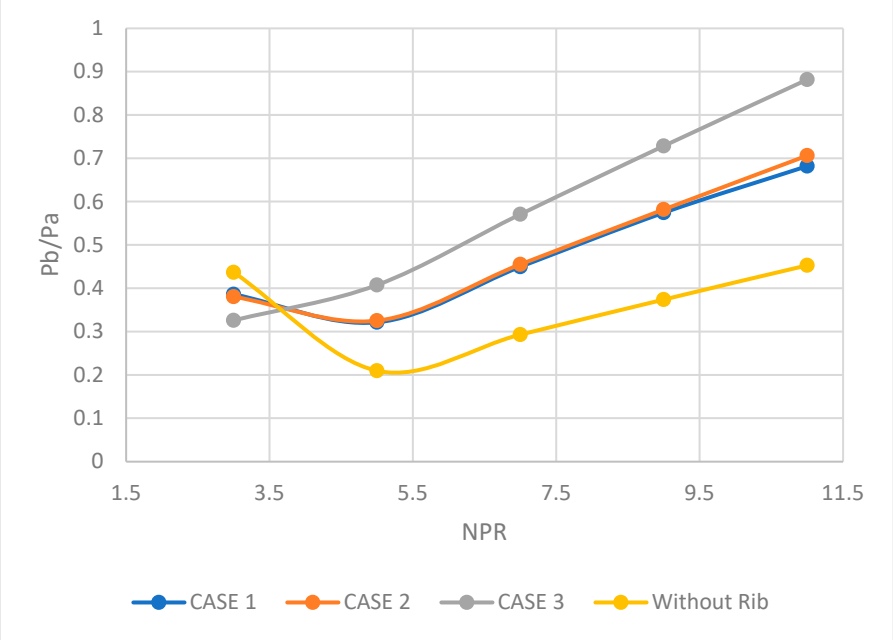

(**b**) L/D = 2

Figure 4: *Cont.*

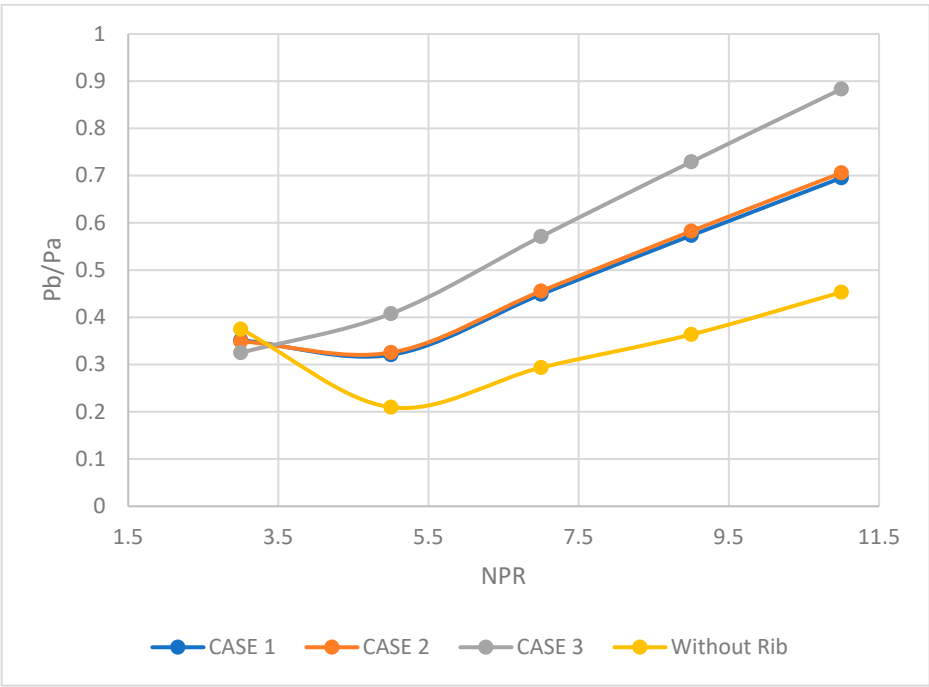

(**c**) L/D = 3

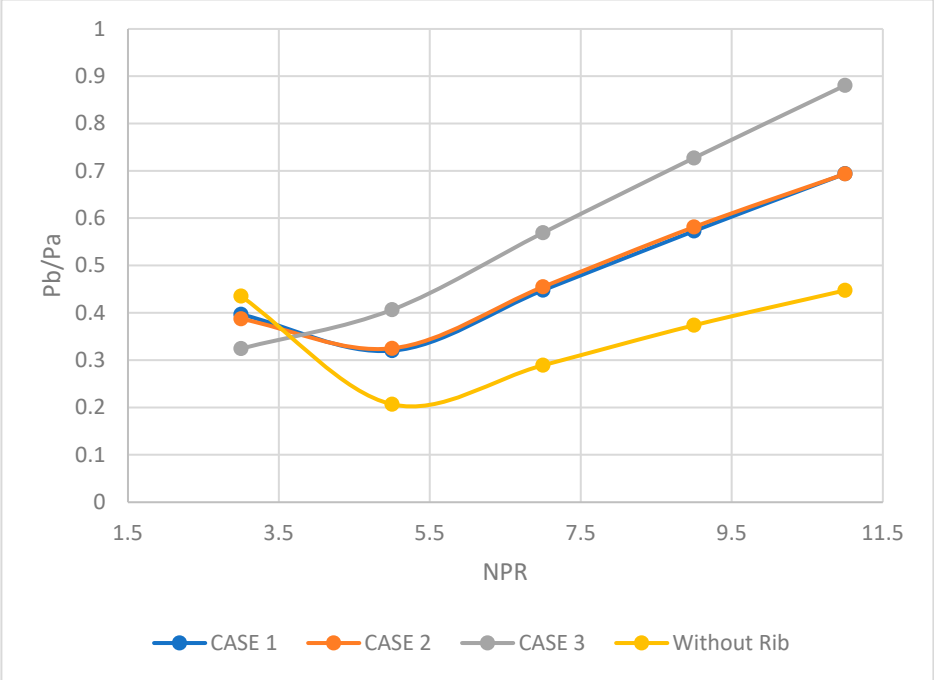

(**d**) L/D = 4

Figure 4: *Cont.*

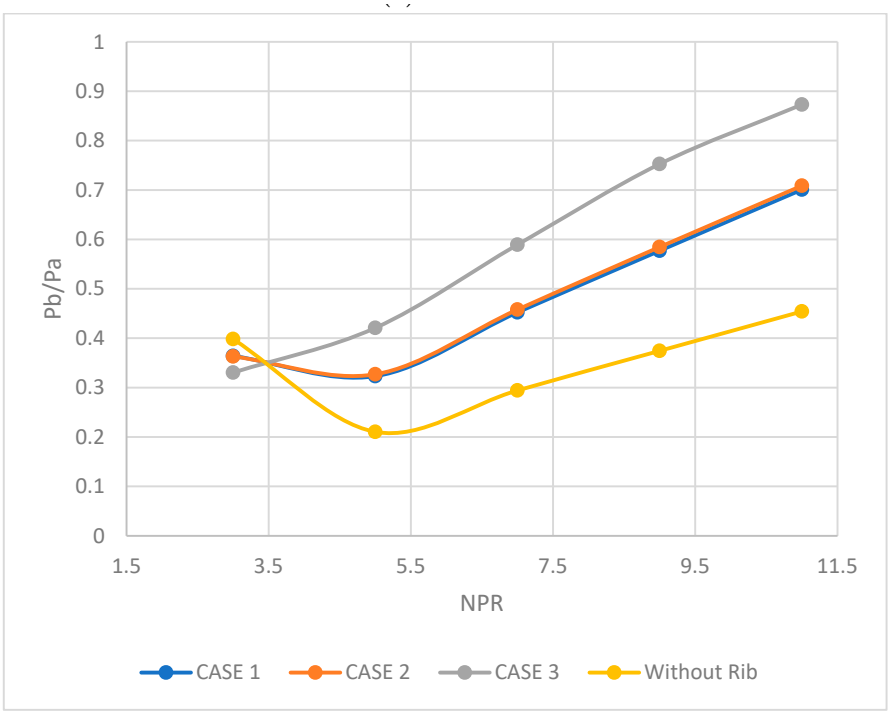

(**e**) L/D = 5

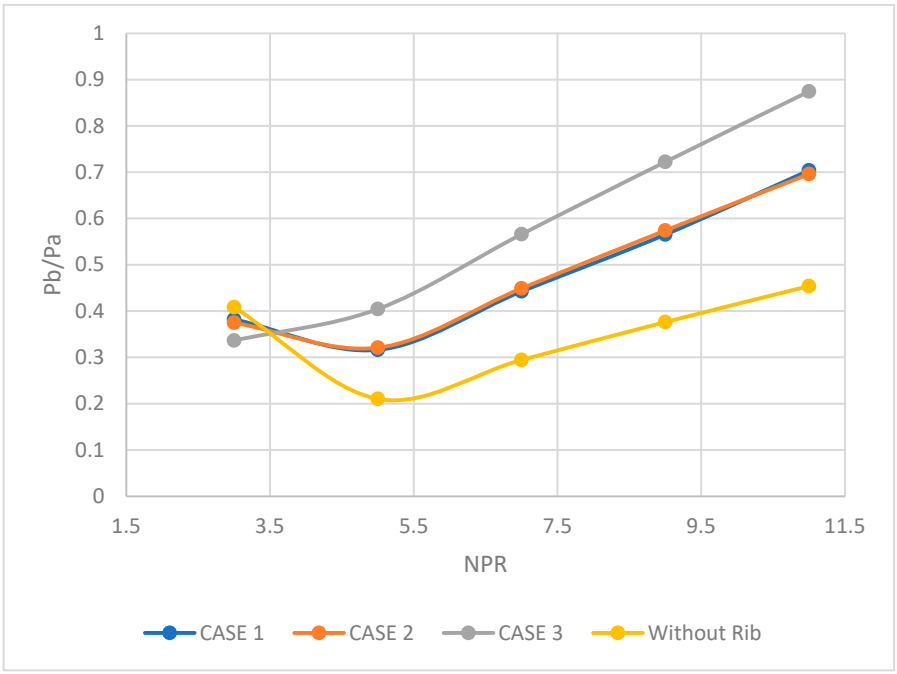

(**f**) L/D = 6

Figure 4: Variation of base pressure with expansion levels for different rib geometries and pipe sizes for rib location at L/D = 0.5.

4.2 Base Pressure Results for Rib Location at L/D = 1

Fig. 5 shows the base pressure results for the control location at L/D = 1 across different rib-geometry cases at various expansion levels. From Fig. 5a, it is evident that for the rib geometries of case 1 and

case 2, as well as for the non-ribbed configuration, the base pressure values are approximately the same. All these results for the stated cases show similar patterns. Specifically, there is an initial decline in base pressure; however, once the flow-accelerating device is operated at the design NPR, the decline stops and base pressure increases substantially. However, for the case 3 rib geometry, the base pressure ratio declines negligibly until NPR reaches 5. When the nozzle is activated at or above the NPR required for ideal expansion, a rectilinear increase in base pressure occurs. These outcomes reiterate that controls, whether active or passive, are effective only when the flow-accelerating device operates under favorable pressure-gradient conditions. From these results, it is evident that, even for three distinct rib geometries, the maximum base pressure is approximately 0.8, indicating that the base pressure remains unequal to atmospheric pressure. Nevertheless, the increase in base pressure is approximately 95%. The other two rib geometries are ineffective, and hence, the base pressure remains the same.

Further, it is observed that for the rib position at L/D = 1, outcomes show that for the duct segment at L/D = 3, there is around a ten percent upsurge in base pressure for NPRs in the range of 3 to 5, and a rise in the base pressure when NPR = 9, as observed in Fig. 5b. Similarly, for a tube span of L/D = 4, at NPR = 3, a 20% reduction in the base pressure ratio is observed; however, when NPR = 5, a negligible growth in the base pressure is observed. This trend is as expected, since at NPR = 3, the nozzle experiences adverse pressure. As NPR increases, the flow regulation by a bullet-shaped rib becomes effective as NPR approaches the design NPR. The findings reiterate that when the nozzle is either appropriately expanded or under-expanded, the control becomes effective. Changes in base pressure were not detected in small pipe segments due to ambient pressure. However, the impact of the ambient conditions will be absent when the stream is attached to the duct wall for larger tube segments, specifically L/D = 5 and 6. It is also observed that once the flow regulator is set to L/D = 0.5, the rib appears to interact with the base vortex, leading to a significant enhancement in base pressure. Due to this, the rib geometries of cases 1 and 2 show a 25% increase in base pressure ratio, whereas the increase in base pressure ratio for the control geometry of case 3 is, by and large, in the same range.

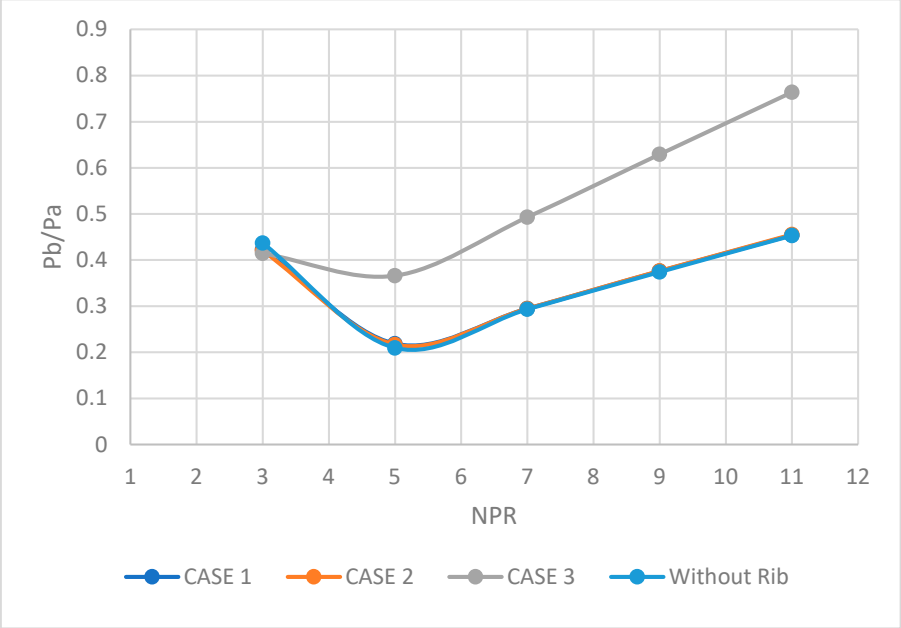

(**a**) L/D = 2

Figure 5: *Cont.*

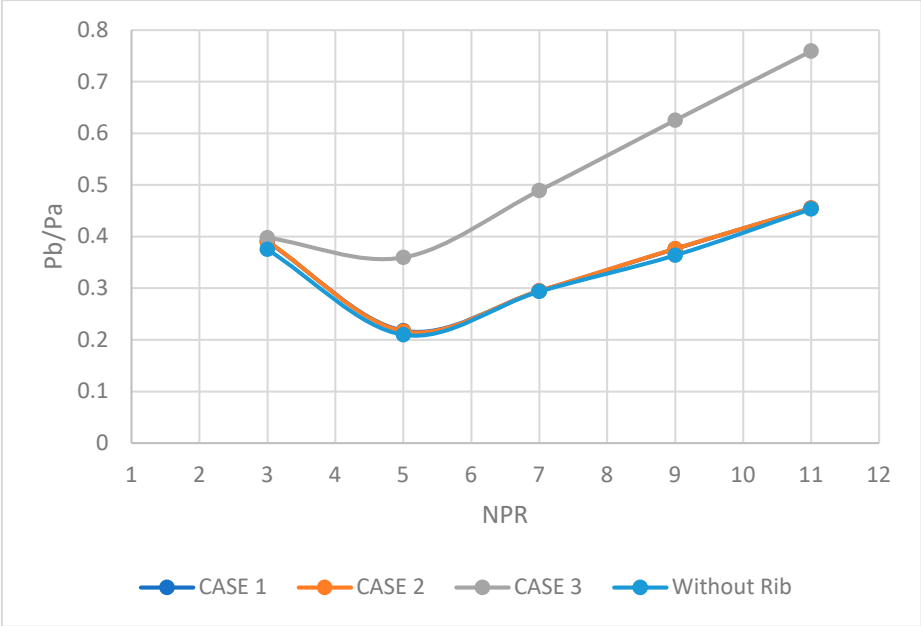

(**b**) L/D = 3

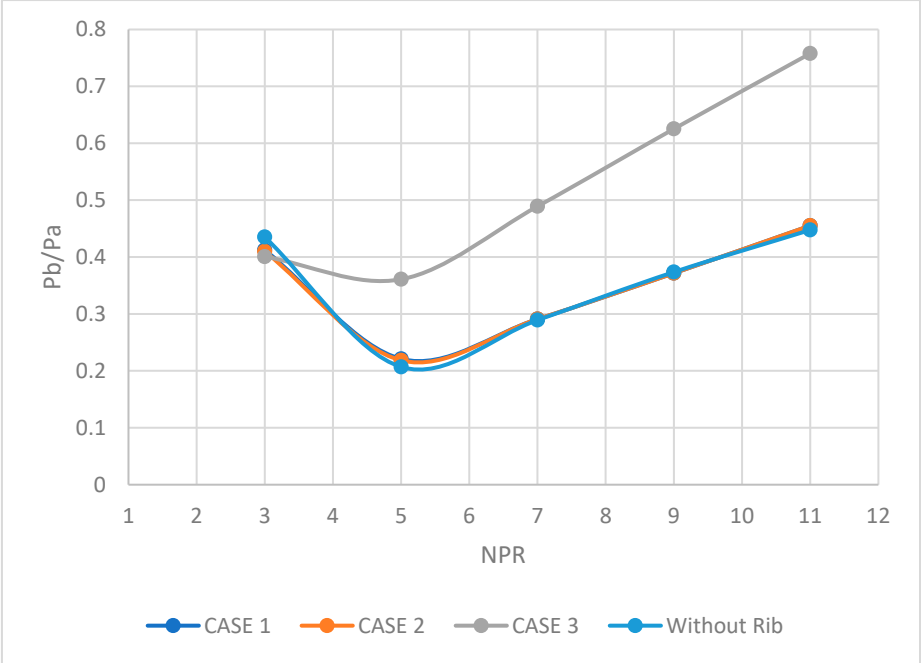

(**c**) L/D = 4

Figure 5: *Cont.*

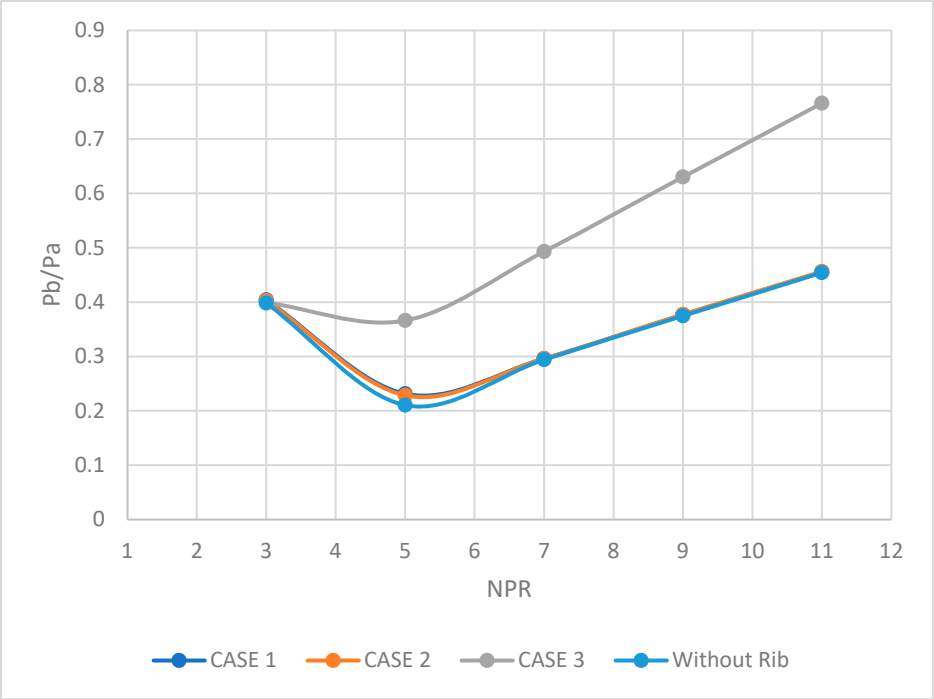

(**d**) L/D = 5

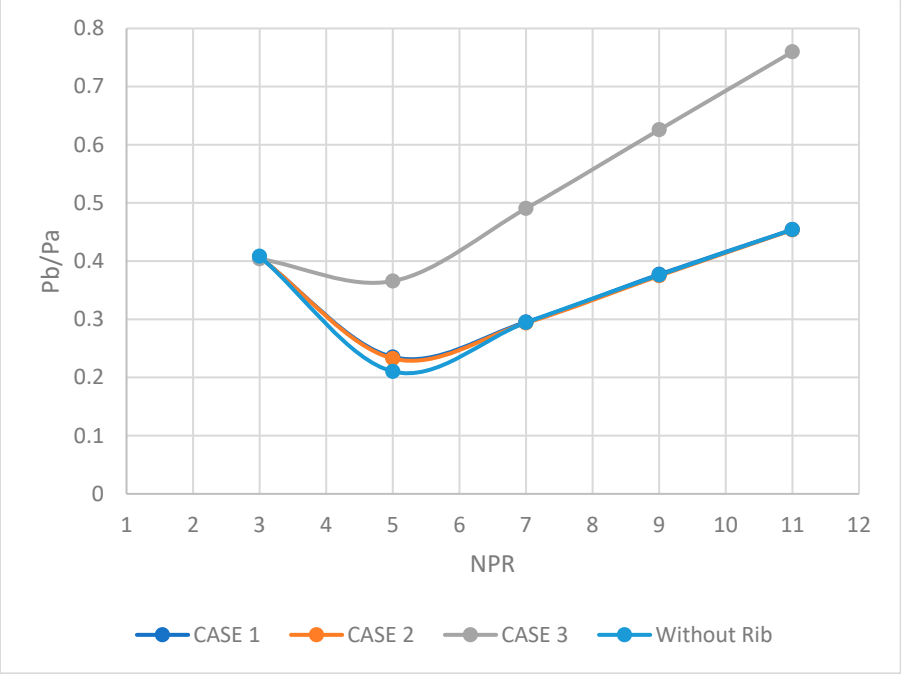

(**e**) L/D = 6

Figure 5: Variation of base pressure with expansion levels for different rib geometries and pipe sizes for rib location at L/D = 0.1.

4.3 Base Pressure Outcomes Intended for Rib Position at L/D = 1.5

For rib placement at L/D = 1.5, the results are presented in Fig. 6 for various expansion levels and duct segments, categorized into three rib types (cases 1, 2, and 3). When the duct segments have an L/D ratio

of 2, the rib geometries assigned to cases 1 and 2 are ineffective. The cause of this tendency is that the reattachment span falls within the range of L/D = 3 to 4. When rib geometry cases 1 and 2 fail to affect the flow, it appears that, for these two rib geometries, there is minimal interaction between the rib and the viscous layer, and any control effect is negated by the reverse flow from the boundary layer. Additionally, for this short duct length, atmospheric pressure will have a substantial impact. However, the rib geometry in case 3 is practical, and the base pressure reaches 0.8 (Fig. 6a), indicating that the base pressure has not yet reached atmospheric pressure.

The findings for pipe segment L/D = 3, regarding the rib geometry of case 3, indicate no change, and the results remain similar for this duct length. However, for the rib geometry of cases 1 and 2, there is a negligible alteration in the base pressure ratio, which remains identical with and without the ribs. This change can be attributed to the tube segment having enlarged and to the shear layer being attached to the pipe wall; hence, the influence of ambient pressure on the flow field in the tube is minimal. Analogous outcomes are observed for L/D = 4, with negligible increases in base pressure for rib geometries 1 and 2. This marginal increase in base pressure is ascribed to the duct length, which further limits the influence of atmospheric pressure. However, the rib geometry results for case 3 remain the same.

While we examine the base-pressure solutions for a duct size of L/D = 5, the rib geometry of case 3 remains unchanged. In addition to a further rise in the duct, a corresponding improvement in base pressure is observed for cases 1 and 2, and a further improvement in base pressure for the control shape in case 3. This further improvement in base pressure values for control cases 1 and 2 is attributed to the large duct span, which restricts the effect of atmospheric pressure. It may be that for any NPR greater than 6, the nozzles are highly under-expanded (Fig. 7b). While the shear layer forms at higher NPRs with a large under-expansion, the flow reattaches farther downstream. Hence, in this area, we may not notice the effect of under-expansion.

While examining the consequences of the investigation for L/D = 6, for rib-geometry cases 1 and 2, a further improvement in base pressure results from the large pipe span and the lower ambient pressure. Only in this pipe span is there a minor pressure intensification at the base region.

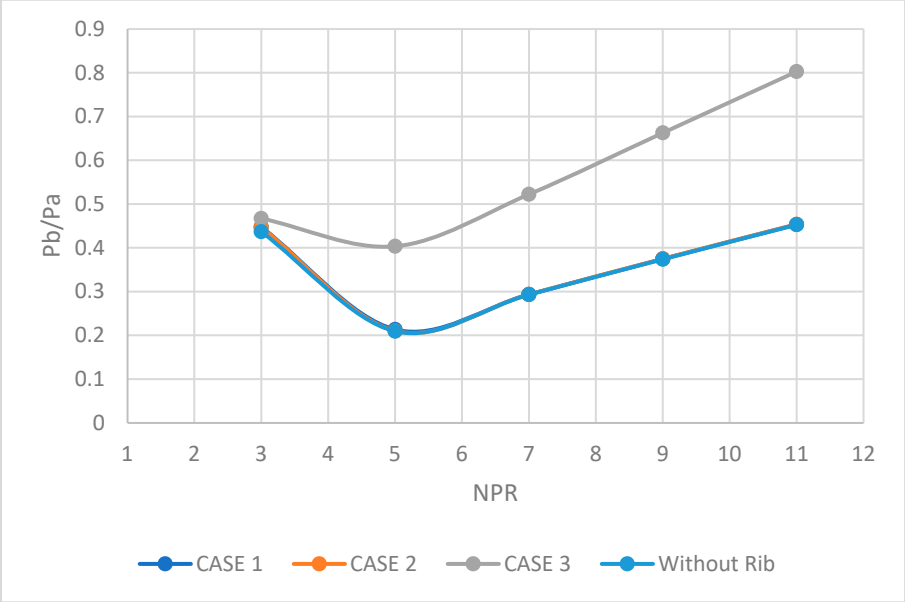

(a) L/D = 2

Figure 6: *Cont.*

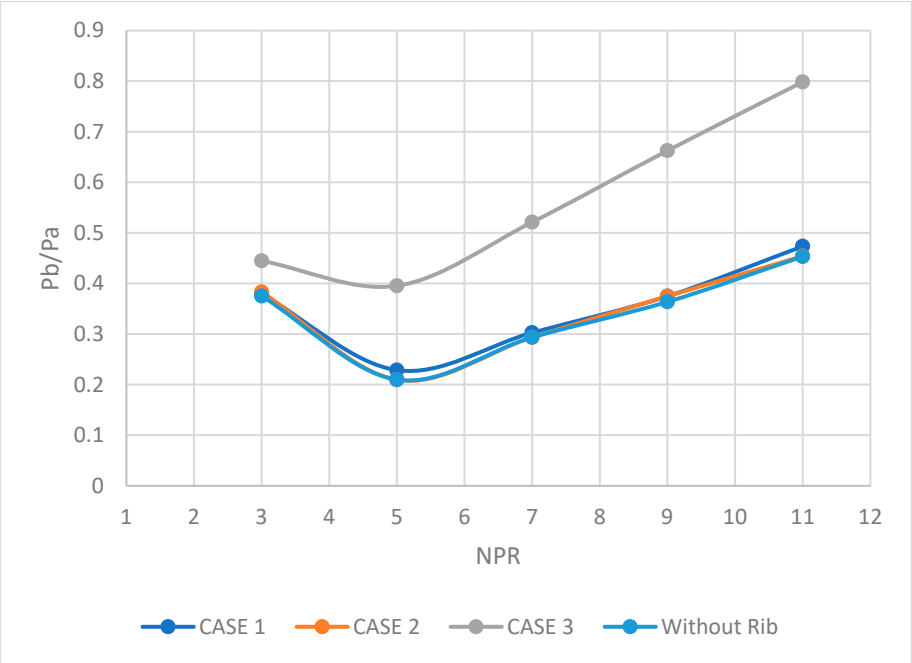

(**b**) L/D = 3

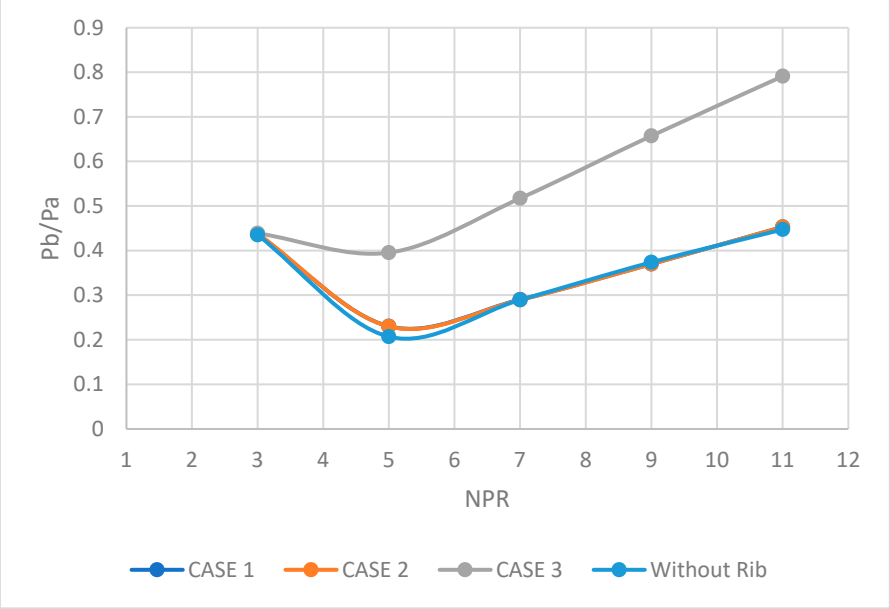

(**c**) L/D = 4

Figure 6: *Cont.*

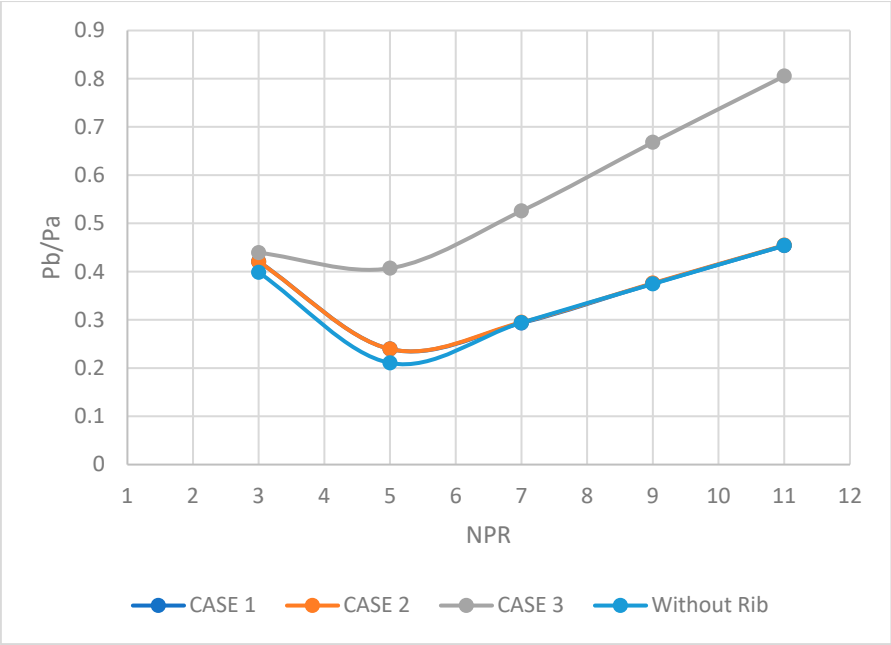

(**d**) L/D = 5

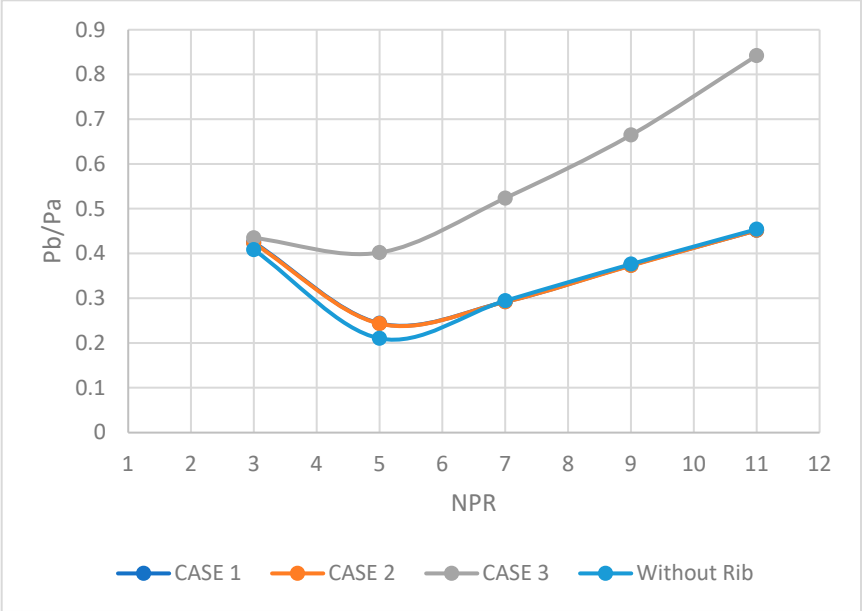

(**e**) L/D = 6

Figure 6: Variation of base pressure with expansion levels for different rib geometries and pipe sizes for rib location at L/D = 1.5.

4.4 Base Pressure Outcomes for Rib Position at L/D = 2.0

The findings, at L/D = 2.0, for the range of NPRs from 3 to 11, are presented for three rib geometries (cases 1, 2, and 3) in Fig. 7. In this case, the ribs are further shifted downstream. In Fig. 7a, it is observed that the pattern of base pressure is very similar to the previous rib locations except for rib geometry case 3; the maximum base pressure value has marginally increased from 0.8 to 0.9, and at the same time, for rib geometry cases 1 and 2, the control is effective only for NPRs ranging from 3 to 6. For NPR values beyond

NPR = 6, the control for rib geometry cases 1 and 2 shows no impact; the base pressures are similar, and the control cannot affect the flow. This phenomenon may be explained as follows.

Analogous outcomes are observed for L/D = 4, with marginal differences in base pressure between the flow regulator geometries in cases 1 and 2 (Fig. 7b). However, the base pressure differs for the control shape in case 3. These changes are attributed to the increase in the pipe span. Similar outcomes are observed for pipe spans with L/D ratios of 5 and 6, as illustrated in Fig. 7c,d.

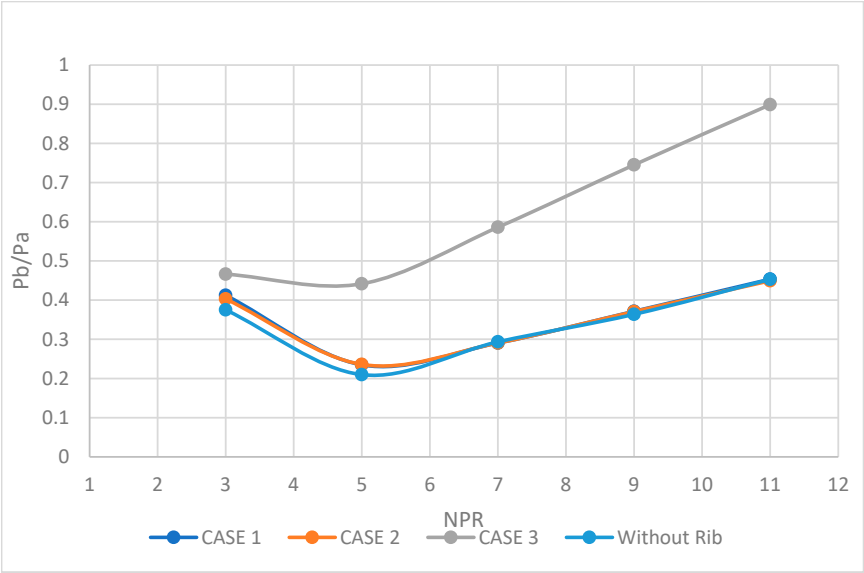

(**a**) L/D = 3

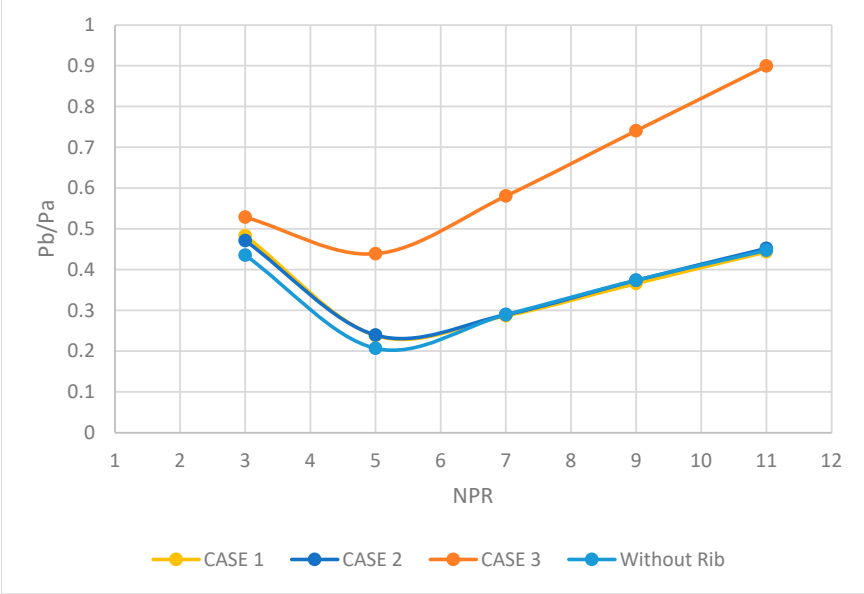

(**b**) L/D = 4

Figure 7: *Cont.*

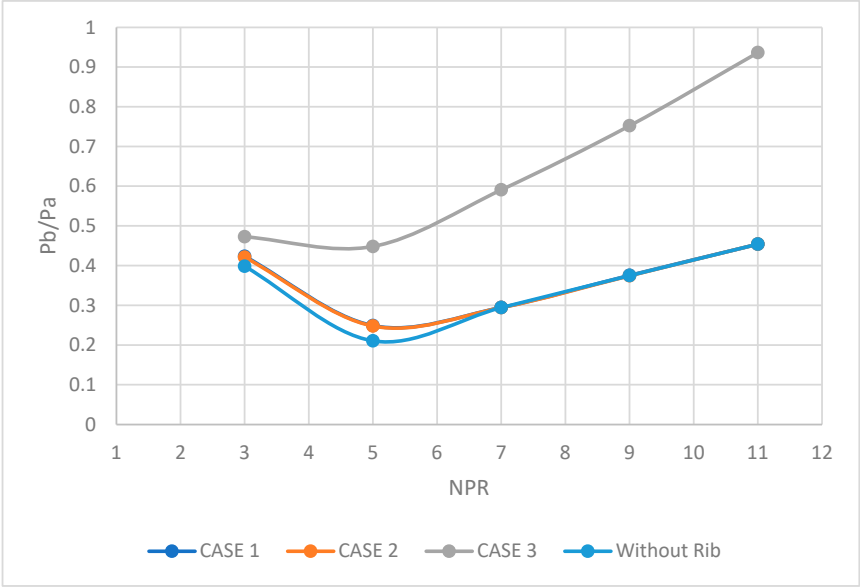

(**c**) L/D = 5

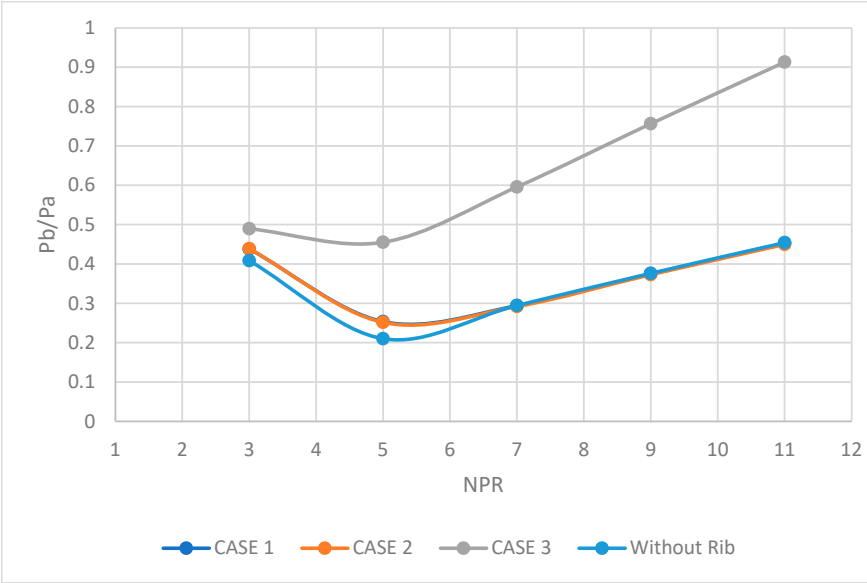

(**d**) L/D = 6

Figure 7: Variation of base pressure with expansion levels for different rib geometries and pipe sizes for rib location at L/D = 2.0.

4.5 Base Pressure Outcomes for Rib Position at L/D = 3.0

When L/D = 3, the findings are presented in Fig. 8 for numerous NPRs (3 to 11) and three different rib geometries. Regarding the two rib geometries (cases 1 and 2), the pattern is nearly identical to that observed in previous cases. However, a nominal increase in the base pressure ratio is observed for the case 3 control geometry, as shown in Fig. 8a. As for base pressure, the control geometries for cases 1 and 2 remained the same, with only marginal variations.

In the present study, with a pipe span of L/D = 5 and a rib position at L/D = 3, case 3 showed a 22% increase in base pressure. For cases 1 and 2, the rib geometry shows a marginal increase in base pressure for NPRs 3 to 6. Because the flow field will be very complex, the flow leaving the nozzle will either be

accompanied by an oblique shock or by an expansion fan. That will make the stream very complex, as evidenced by the results we observe, which are the outcome of the flow. There may be a rise in base pressure, but because of the stream's compression and expansion, the net result can sometimes be zero, depending on the balance of positive and negative effects. This phenomenon is observed during base-flow control by microjets, where we found that the jet noise disappeared and the supersonic flow at Mach 1.8 became silent. Similar results for duct size (L/D = 6) are observed for rib placement at L/D = 3; base pressure remains unchanged, indicating that changes in duct length do not affect it. That may be because the flow is attached to the duct. Also, there is no effect on the stream owing to atmospheric pressure.

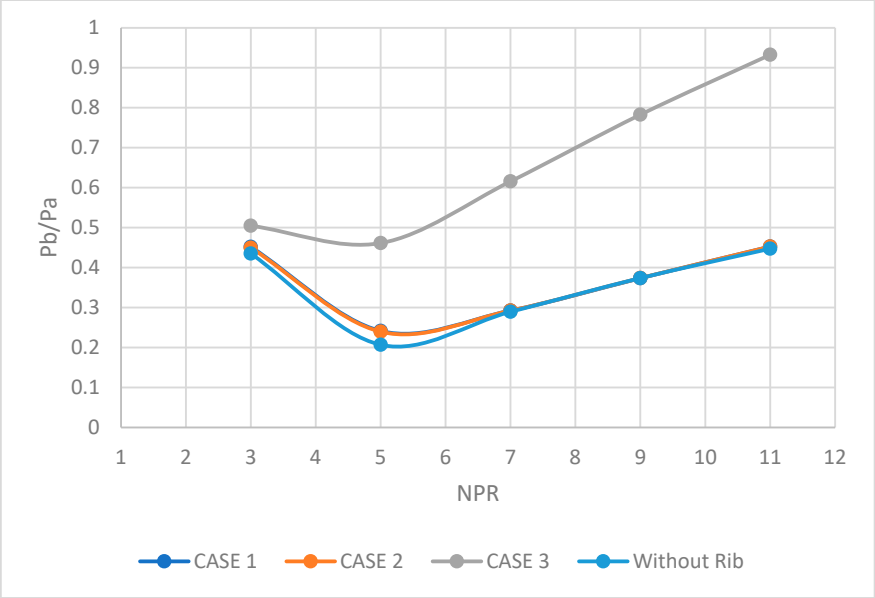

(**a**) L/D = 4

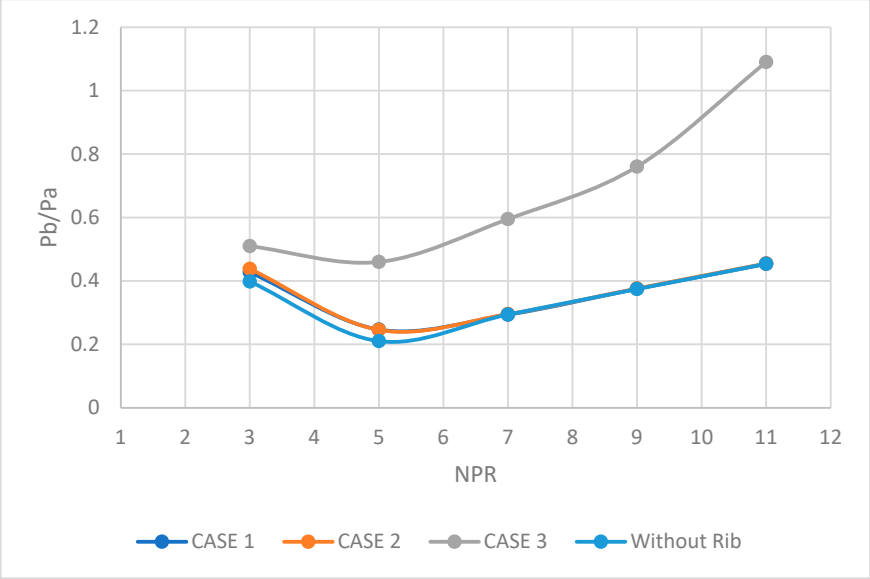

(**b**) L/D = 5

Figure 8: *Cont.*

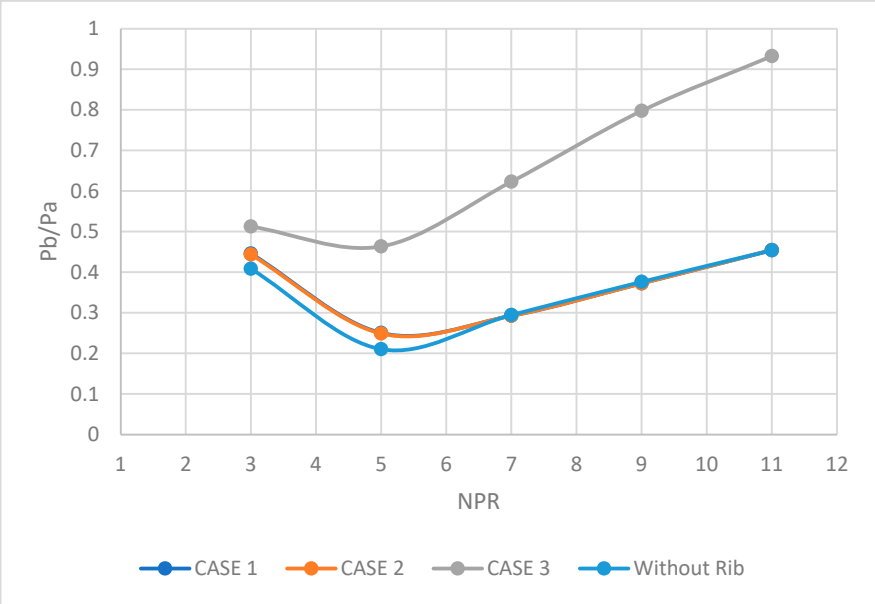

(**c**) L/D = 6

Figure 8: Variation of base pressure with expansion levels for different rib geometries and pipe sizes for rib location at L/D = 3.0.

4.6 Base Pressure Outcomes for Rib Position at L/D = 4

The results for the control position at L/D = 4 across multiple expansion levels are shown in Fig. 9. The flow shape is identical to that observed at the other rib positions. From the findings, it is evident that for ribs 1 and 2, NPRs in the range of 3 to 5 results in minimal growth in base pressure, which is later offset by higher NPRs. The flow regulation via bullet ribs in cases 1 and 2 is inadequate. However, the case 3 combination of bullet rib geometry is effective from NPR 5 onward, and the control is effective as well. The physical reasons for this trend in the base pressure could be that, in cases 1 and 2, the former vortices are counterproductive, and control does not lead to an increase in the base pressure. However, in the third rib option, secondary vortices form, and the reattachment lengths are such that the flow reattaches beyond the optimum reattachment length due to the larger area ratio. Hence, the relief available to the flow adds mass to the base, increasing the base pressure. Thus, we can say that rib geometry and its dimensions play a substantial part in regulating base pressure.

4.7 Contours at Various NPRs

4.7.1 Over-Expanded Duct

In this study, although we generated a large volume of contour data, we present only a few cases to limit the manuscript length. Fig. 10a shows the velocity contours for NPR = 3; at NPR 3, the nozzle is over-expanded. When the flow is exhausted, it decelerates; however, the main jet carries maximum kinetic energy. The jet exits over-expanded and decelerates downstream, but a compact high-speed core persists along the centerline, bounded by growing shear layers. The bullet-shaped rib accelerates flow over its forebody and induces a separated, low-velocity wake immediately downstream. The shear layer thickens as it interacts with the rib-induced wake and the base-corner recirculation, promoting momentum exchange toward the near-wall region. Similarly, the pressure contours indicate that the exit pressure is initially low and later recovers, as shown in Fig. 10b. Static pressure is initially low at the nozzle exit and recovers

progressively downstream, indicating shock-induced/compressive adjustment of the over-expanded jet. A high-pressure footprint appears on the rib's upstream face due to flow impingement and local stagnation; a corresponding low-pressure pocket forms in the rib wake. Near the base corner, pressure is depressed within the recirculation cell but rises as mixing and reattachment proceed, evidencing net pressure recovery along the duct.

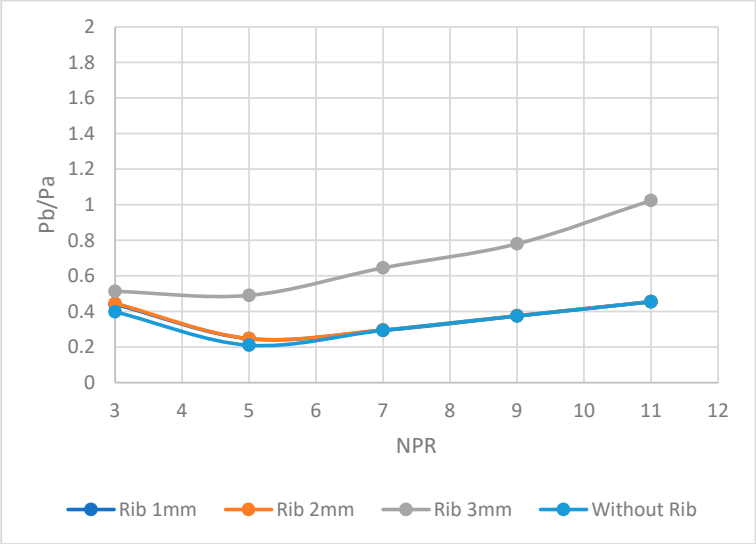

(**a**) L/D = 5

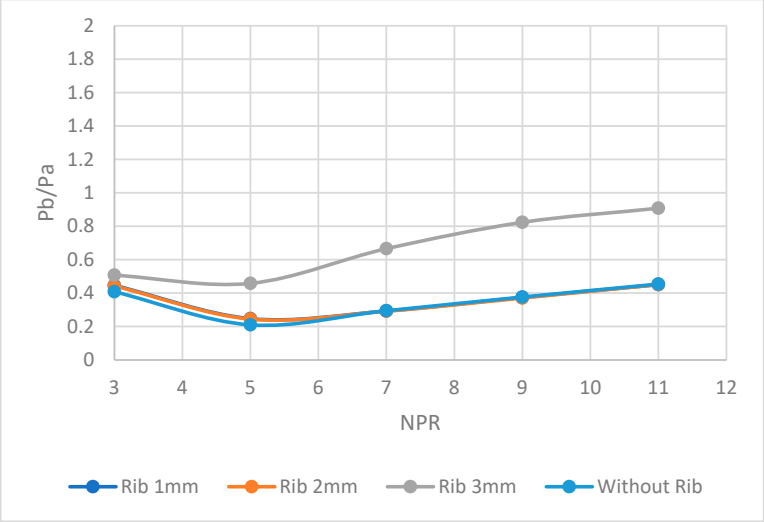

(**b**) L/D = 6

Figure 9: Variation of base pressure with expansion levels for different rib geometries and pipe sizes for rib location at L/D = 4.0.

In Fig. 10c, the streamline contour indicates two recirculation zones: one at the base corner and the other near the bullet-shaped rib. The rib-wake cell interacts with the base-corner cell through the intervening shear layer, intermittently feeding low-momentum fluid into the base region while also shielding it from direct jet entrainment. The combined effect promotes earlier mixing and aids pressure recovery without causing wholesale jet deflection. The rib at L/D = 0.5 triggers-controlled separation and a stable wake, which, together with the base-corner bubble, supports a base-pressure rise under over-expanded

conditions. Pressure recovery downstream suggests that the duct span at L/D = 6 is adequate for flow reattachment and near uniformity; additional length is unlikely to yield substantial gains at this NPR.

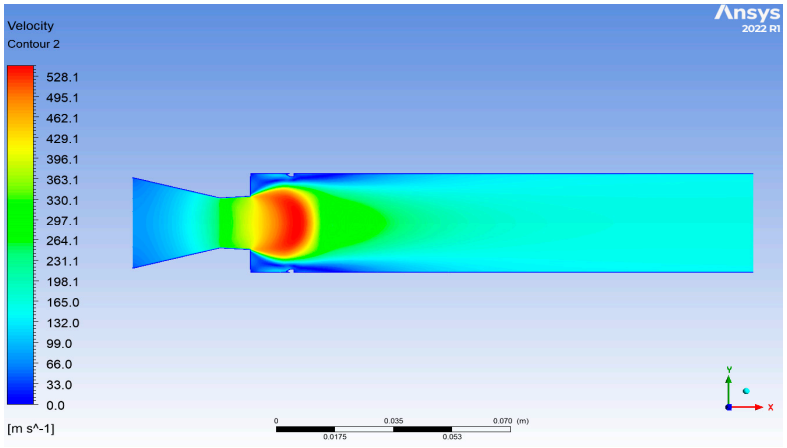

(**a**) Velocity contour

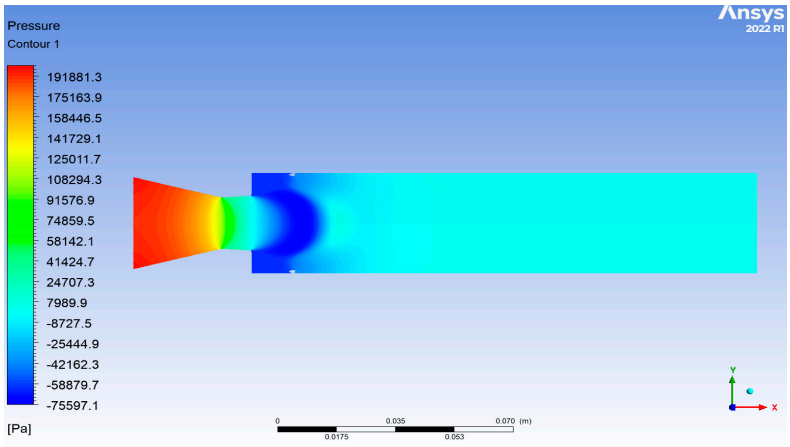

(**b**) Pressure contour

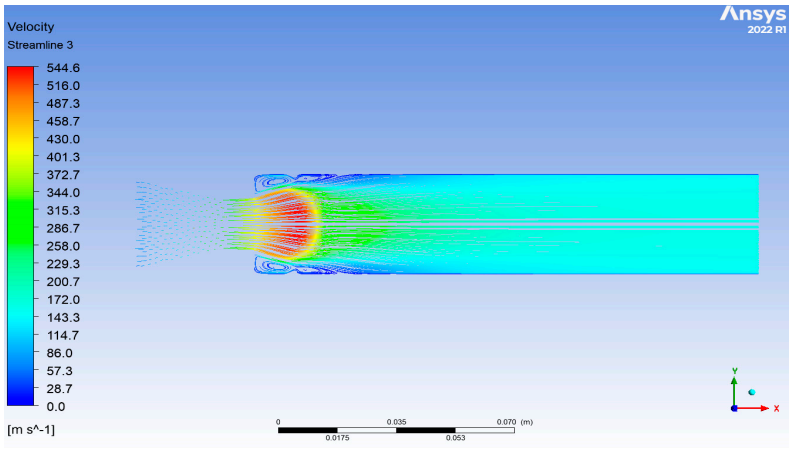

(**c**) Streamline contour

Figure 10: Contours at NPR = 3, L/D = 6 for rib position L/D = 0.5.

4.7.2 Under-Expanded Duct

Fig. 11a–c shows the contour plots for velocity, pressure, and streamlines for NPR = 7, a pipe span of 150 mm, and a rib situated at L/D = 0.5. The flow from the nozzle into the pipe is favorable. The consequences of the expansion level are shown by contours of velocity and pressure, as well as by streamlines.

The jet issues under-expanded; expansion near the lip accelerates the core, followed by gradual decay and partial shock-cell modulation (weak alternating bands), damped by confinement. Approaching the rib, the flow accelerates over the foreface and then separates to form a low-speed wake immediately downstream. The shear layer thickens and is deflected toward the wall by the rib-induced wake, promoting earlier near-wall momentum exchange and aiding reattachment further downstream. By the downstream half of the duct, the velocity field becomes more uniform, indicating substantial mixing and attenuation of core oscillations.

Static pressure is initially above ambient at the exit (under-expanded), then drops across expansion waves and partially recovers downstream through recompression. A clear stagnation/high-pressure region forms on the rib's upstream face, with a low-pressure pocket in the wake; this pressure differential drives enhanced entrainment and mixing. Alternating mild high- and low-pressure patches along the centerline are consistent with a damped shock-cell pattern; amplitudes decrease downstream due to wall confinement and rib interaction. Base-corner pressure is depressed near the separation bubble but recovers progressively toward the reattachment region.

Two primary recirculation zones are visible: a base-corner bubble and a compact rib-wake bubble just downstream of the rib. The wake bubble intermittently feeds low-momentum fluid toward the base while shielding it from direct jet entrainment; their interaction thickens the shear layer and accelerates pressure recovery. Streamlines remain aligned mainly with the duct axis downstream, indicating no large-scale jet deflection despite localized separation, implications for base-pressure control. Under under-expanded conditions, the rib at L/D = 0.5 establishes a stable wake that, together with the base-corner bubble, enhances mixing and supports a net rise in base pressure. The velocity and pressure fields suggest that reattachment and near uniformity are largely achieved at L/D = 3; beyond this length, further duct length would yield diminishing gains at NPR = 7.

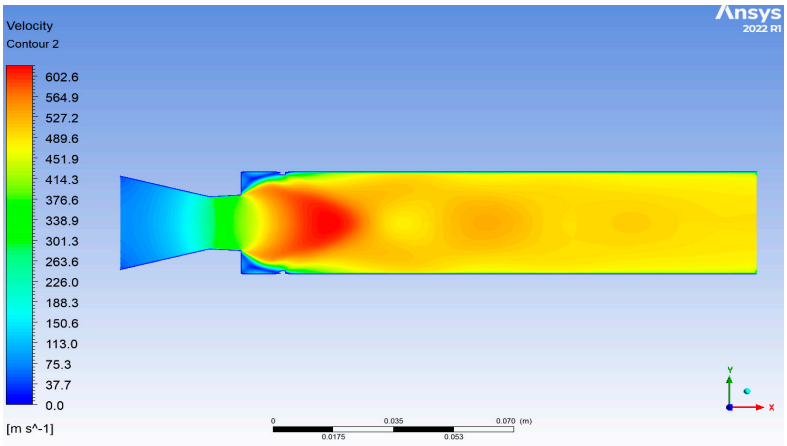

(**a**) Velocity contours

Figure 11: *Cont.*

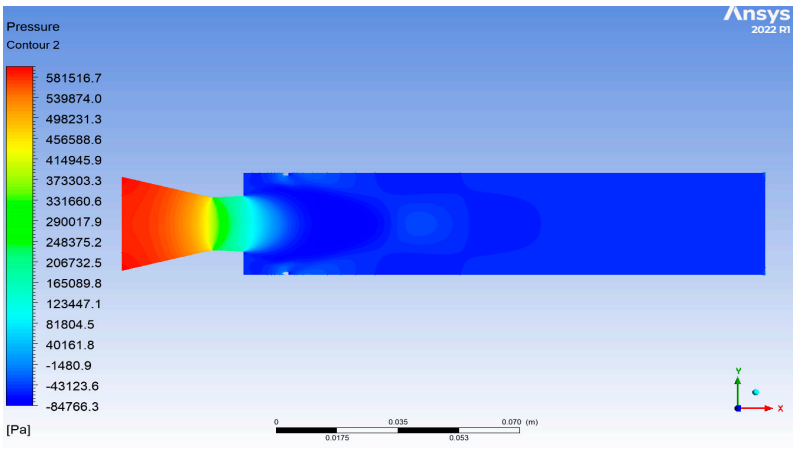

(**b**) Pressure contours

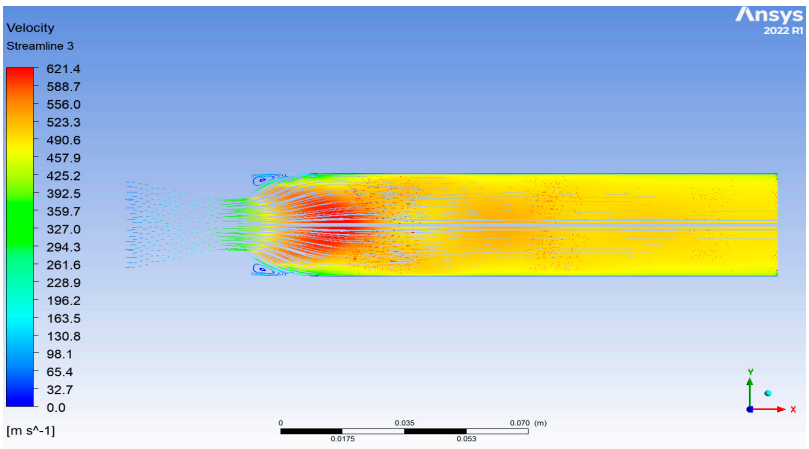

(**c**) Streamline contours

Figure 11: Contours at NPR = 7, L/D = 6 for rib location at L/D = 0.5.

5 Conclusion

Base-pressure control is governed primarily by rib placement and geometry. Positioning a rib at L/D = 0.5 promotes interaction with the base vortex, yielding a 25% increase in base pressure for geometries 1 to 2. In contrast, geometry 3 produces a significantly larger 95% increase, which is largely insensitive to placement over L/D from 0.5 to 1.5. The augmentation peaks near the reattachment region (L/D from 2 to 3), yielding a roughly 30% increase in the base-pressure ratio at or slightly above unity; this is attributed to strong interactions between secondary vortices that drive additional mass toward the base. Across NPR, the range is 3 to 11, with the control at L/D = 3. Cases 1 and 2 follow the same trend, and case 3 shows a modest additional gain. When the duct span is L/D = 5 and the rib is positioned at L/D = 3, case 3 achieves 22% growth, while case 1 and 2 exhibit only marginal increases (notably at NPR 3 to 6). Compression and expansion structures can offset each other, sometimes yielding a negligible net change. Extending the duct to L/D = 6 for the rib position at L/D = 3 shows no further effect, indicating limited sensitivity to duct length once attachment is established. A rib at L/D = 4 has a negligible influence. Overall, meaningful augmentation requires careful choice of rib geometry and placement near the base vortex or reattachment; outside these zones or at larger duct lengths, gains diminish.

Acknowledgement: This research is supported by the Structures and Materials (S&M) Research Lab of Prince Sultan University, and the authors acknowledge Prince Sultan University's support in paying the article processing charges (APC) for this publication.

Funding Statement: The authors received no specific funding for this study.

Author Contributions: The authors confirm contribution to the paper as follows: study conception and design: Uzma Anis Takkalki and Sayed Ahmed Imran Bellary; data collection: Sher Afghan Khan; analysis and interpretation of results: Sher Afghan Khan, Abdul Aabid and Muneer Baig; draft manuscript preparation: Uzma Anis Takkalki and Sayed Ahmed Imran Bellary. All authors reviewed and approved the final version of the manuscript.

Availability of Data and Materials: Data will be made available on request.

Ethics Approval: Not applicable.

Conflicts of Interest: The authors declare no conflicts of interest.

References

1. Khan A, Mazlan NM, Sulaeman E. Effect of ribs as passive control on base pressure at sonic Mach numbers. CFD Lett. 2022;14(1):140–51. [CrossRef].
2. Khan A, Mazlan NM, Ismail MA. Numerical simulation of suddenly expanded flow from a converging nozzle at sonic Mach number. In: Proceedings of the International Conference of Aerospace and Mechanical Engineering 2019: AeroMech 2019; 2019 Nov 20–21; Nibong Tebal, Malaysia. p. 349–59. [CrossRef].
3. Khan A, Akhtar MN, Aabid A, Baig M, Khan SA. Comprehensive CFD analysis of base pressure control using quarter ribs in a sudden expansion duct at sonic Mach numbers. Int J Thermofluids. 2024;24:100908. [CrossRef].
4. Li S, Li L, Huang W, Zhao Y, Chen J. Design and investigation of an equal cone-variable Mach number wave rider in hypersonic flow. Aerosp Sci Technol. 2020;96:105540. [CrossRef].
5. Rathakrishnan E, Ramanaraju OV, Padmanaban K. Influence of cavities on suddenly expanded flow field. Mech Res Commun. 1989;16(3):139–46. [CrossRef].
6. Pandey KM, Rathakrishnan E. Influence of cavities on flow development in sudden expansion. Int J Turbo Jet Engines. 2006;23(2):97. [CrossRef].
7. Vikramaditya NS, Viji M, Verma SB, Ali N, Thakur DN. Base pressure fluctuations on a typical missile configuration in the presence of a base cavity. J Spacecr Rocket. 2017;55:1–11. [CrossRef].
8. Baig MA, Al-Mufadi F, Khan SA, Rathakrishnan E. Control of base flows with microjets. Int J Turbo Jet Engines. 2011;28(1):59–69. [CrossRef].
9. Rehman S, Khan SA. Control of base pressure with micro-jets: Part I. Aircr Eng Aerosp Technol. 2008;80(2):158–64. [CrossRef].
10. Rao GR, Ramakanth US, Lakshman A. Flow analysis in a convergent-divergent nozzle using CFD. Int J Res Mech Eng. 2013;1(1):136–44.
11. Najar NA, Dandotiya D, Najar FA. Comparative analysis of k-ε and Spalart-Allmaras turbulence models for compressible flow through a convergent-divergent nozzle. Int J Eng Sci. 2013;2(8):8–17.
12. Salvador FJ, Jaramillo D, Romero JV, Roselló MD. Using a homogeneous equilibrium model for the study of the inner nozzle flow and cavitation pattern in convergent-divergent nozzles of diesel injectors. J Comput Appl Math. 2017;309(2):630–41. [CrossRef].
13. Pushpa BV, Sankar M, Mebarek-Oudina F. Buoyant convective flow and heat dissipation of Cu–H_2O nanoliquids in an annulus through a thin baffle. J Nanofluids. 2021;10:292–304. [CrossRef].
14. Koomullil R, Soni B, Singh R. A comprehensive generalized mesh system for CFD applications. Math Comput Simul. 2008;78(5–6):605–17. [CrossRef].
15. Rathakrishnan E. Effect of ribs on suddenly expanded flows. AIAA J. 2001;39(7):1402–4. [CrossRef].
16. Aabid A, Khan SA. Investigation of high-speed flow control from cd nozzle using design of experiments and cfd methods list of symbols. Arab J Sci Eng. 2021;46(3):2201–30. [CrossRef].